

# Survey of instability thresholds of flow between exactly counter-rotating disks

By **C. NORE**<sup>1,2</sup>, **M. TARTAR**<sup>2</sup>, **O. DAUBE**<sup>3</sup>  
AND **L. S. TUCKERMAN**<sup>2</sup>

<sup>1</sup>Université Paris XI, Département de Physique, 91405 Orsay Cedex France

<sup>2</sup>Laboratoire d'Informatique pour la Mécanique et les Sciences de l'Ingénieur, CNRS, BP 133, 91403 Orsay Cedex France

<sup>3</sup>Université d'Evry Val d'Essonne, 40 rue du Pelvoux, 91020 Evry Cedex France

(Received ?? and in revised form ??)

The three-dimensional linear instability of axisymmetric flow between exactly counter-rotating disks is studied numerically. The dynamics are governed by two parameters, the Reynolds number  $Re$  based on cylinder radius and disk rotation speed and the height-to-radius ratio  $\Gamma$ . The stability analysis performed for  $0.5 \leq \Gamma \leq 3$  shows that non-axisymmetric modes are dominant and stationary and that the critical azimuthal wavenumber is a decreasing function of  $\Gamma$ . The patterns of the dominant perturbations are analysed and a physical mechanism related to a shear layer instability is discussed. No evidence of complex dynamical behavior is seen in the neighborhood of the 1:2 codimension-two point when the  $m = 2$  threshold precedes that of  $m = 1$ . Axisymmetric instabilities are also calculated; these may be stationary or Hopf bifurcations. Their thresholds are always higher than those of non-axisymmetric modes.

---

## 1. Introduction

The flow above a rotating disk and between rotating disks in a cylindrical cavity, or von Kármán swirling flow (Zandbergen & Dijkstra (1987)), was first studied by von Kármán (1921) and Batchelor (1951) and occurs frequently in geophysical situations such as in atmospheric eddies and in industrial applications such as in turbomachines. It depends qualitatively on the height-to-radius aspect ratio  $\Gamma$ , as well as on the ratio  $s$  of the angular velocities of the upper and lower disks.

Most studies have focused on the rotor-stator configuration with  $s = 0$ . For  $\Gamma = O(1)$ , attention was initially devoted to the possible appearance of axisymmetric recirculation zones on the cylinder axis called vortex breakdown. These bubbles do not seem to result from an instability but rather from a continuous evolution of the basic state. As computational capabilities have increased, interest has turned to the breaking of axisymmetry (e.g. Spohn, Mory & Hopfinger (1998), Sotiropoulos & Ventikos (1998), Sotiropoulos & Ventikos (2001), Blackburn & Lopez (2000), Blackburn & Lopez (2002), Gelfgat, Bar-Yoseph & Solan (2001), Lopez, Marques & Sanchez (2001)). Gelfgat, Bar-Yoseph & Solan (2001) performed a linear stability analysis of the steady axisymmetric base flow in the range  $\Gamma \in [1, 3.5]$  and found that, for  $1.63 \leq \Gamma \leq 2.76$ , the first bifurcation is to an axisymmetric and oscillatory state. Outside this range, the instability is not axisymmetric and azimuthal wavenumbers  $m = 2, 3$  or  $4$  dominate.

When  $\Gamma \ll 1$  and  $s = 0$ , the dynamics are dominated by the boundary layer instabilities, namely the Ekman and Bödewadt boundary layers, in the neighborhood of

the rotating and the stationary disk, respectively (e.g. Schouveiler, Le Gal & Chauve (1998), Gauthier, Gondret & Rabaud (1999), Schouveiler, Le Gal & Chauve (2001), Serre, Crespo del Arco & Bontoux (2001)). Instabilities occur in the form of propagating spirals or circular vortices. These boundary layer instabilities are of two types (I and II, or B and A) and thought to be related to an unstable inflection point, and to the Coriolis force, respectively. They have been extensively studied, both experimentally, and theoretically within the framework of the self-similar von Kármán equations for flow above a single rotating disk; see e.g. Faller (1991), Pikhtov & Smirnov (1993) and references cited in Schouveiler, Le Gal & Chauve (2001). (Gauthier *et al.* (2002) observed similar patterns in the corotating configuration  $s > 0$  and in some weakly counter-rotating cases.)

The counter-rotating case  $s < 0$  has recently opened a new area of study. In this case, instabilities arise in the free shear layer lying between two regions of opposite azimuthal velocities. Lopez *et al.* (2002) have varied  $s$  between 0 and  $-0.8$ , for  $\Gamma = 0.5$  and  $Re = 1000$  and have observed rotating waves in the form of funnel-like vortices with azimuthal wavenumbers 4 and 5, as well as more complicated dynamics. For  $\Gamma \sim 0.05$  Gauthier *et al.* (2002) also observed a new pattern of spirals, which roll up towards the center in the direction opposite to that of the faster disk. They suggested that this spiral structure is engendered by the same free shear layer instability as in Lopez *et al.* (2002). Moisy *et al.* (2003) confirmed this hypothesis with an experimental study in the range  $\Gamma \in [1/20.9, 1/3.8]$  and  $s \in [-1, -0.135]$ , in which the pattern consists of vertical vortices surrounded by these negative spirals. At moderate  $\Gamma$  and/or large Reynolds numbers, the vortices are preferred while, at small  $\Gamma$  and/or small  $Re$ , the negative spirals dominate.

In a previous paper (Nore *et al.* (2003)), we have studied the exactly counter-rotating case,  $s = -1$ , at a fixed aspect ratio  $\Gamma = 2$ . We have shown that, when the disk rotation rate is increased, the axisymmetric basic state becomes unstable through a Kelvin-Helmholtz instability of the equatorial azimuthal free shear layer created by the counter rotation of the top and bottom disks. This instability gives rise to steady states with one or two corotating radial vortices and is accompanied by more complex dynamics like traveling waves, modulated traveling waves, and near-heteroclinic cycles.

The main purpose of this paper is to study the linear threshold of the order parameter, the Reynolds number, when varying the aspect ratio  $\Gamma$  and keeping  $s = -1$ , i.e. the bottom and top disks are exactly counter-rotating. The outline of the paper is as follows: in § 2, the problem is formulated, along with its symmetries; § 3 summarizes the numerical methods and code validation. In § 4.1, the non-axisymmetric thresholds for bifurcations from the basic axisymmetric state are reported, together with the patterns of the eigenvectors. The physical mechanism is interpreted in § 4.2 as a manifestation of the Kelvin-Helmholtz instability as previously suggested in Nore *et al.* (2003). In § 4.3, we investigate the nonlinear behavior of the azimuthal modes  $m = 2$  and  $m = 1$  near their codimension-two point, in light of the complex dynamical states observed in Nore *et al.* (2003). The axisymmetric thresholds are studied in § 5 although the  $m = 0$  mode is never the most unstable: up to two real and two complex eigenvalues interact, leading to a variety of different bifurcations. § 6 contains our conclusion.

## 2. Formulation of the problem

### 2.1. The governing equations

We consider a cylindrical cavity of radius  $R$  and height  $H$  filled with an incompressible fluid of kinematic viscosity  $\nu$  and density  $\rho = 1$ . The motion is driven by the upper and lower disks rotating at constant angular velocity  $\Omega_{\text{up}}$  and  $\Omega_{\text{low}}$ , respectively. The

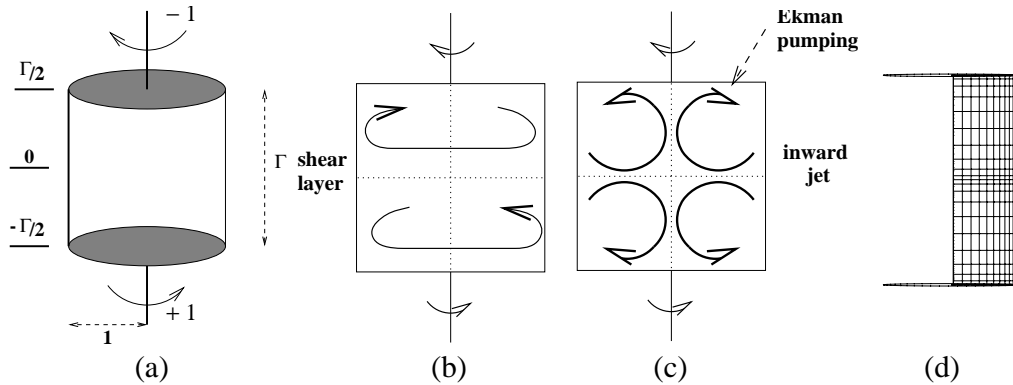


FIGURE 1. (a) Sketch of the flow geometry in non dimensionalised units. (b) Equatorial shear layer separating two regions of opposite azimuthal velocities. (c) Recirculation zones due to Ekman pumping meet, forming a radially inward jet. (d) The non-uniform grid in the  $(r, z)$  plane used for computations at  $\Gamma = 3$ . For clarity, only one out of five points is represented in each direction.

dimensionless momentum and continuity equations read

$$\frac{\partial \mathbf{v}}{\partial t} + (\mathbf{v} \cdot \nabla) \mathbf{v} = -\nabla p + \frac{1}{\text{Re}} \nabla^2 \mathbf{v}, \quad (2.1a)$$

$$\nabla \cdot \mathbf{v} = 0 \quad (2.1b)$$

where  $\mathbf{v}$  is the velocity,  $p$  the pressure, and  $\text{Re} = \Omega_{\text{low}} R^2 / \nu$  the Reynolds number. The velocity, pressure, length and time are non dimensionalised by  $\Omega_{\text{low}} R$ ,  $\rho(\Omega_{\text{low}} R)^2$ ,  $R$  and  $1/(2\pi\Omega_{\text{low}})$  (the rotation period), respectively. Two supplementary non-dimensional parameters are the aspect ratio  $\Gamma = H/R$  and the angular velocity ratio  $s = \Omega_{\text{up}}/\Omega_{\text{low}}$ . We study the case where the disks rotate at exactly opposite angular velocities, namely  $s = -1$ , and vary the aspect ratio. The flow geometry is sketched on figure 1a.

The boundary conditions on the cylinder walls are:

$$\mathbf{v} = 0 \quad \text{on the stationary sidewall at } r = 1 \quad (2.2a)$$

$$\mathbf{v} = \pm r \mathbf{e}_\theta \quad \text{on the rotating disks at } z = \pm \Gamma/2 \quad (2.2b)$$

## 2.2. Symmetries

Figure 1 depicts the basic axisymmetric steady flow, which consists of a predominant equatorial shear layer produced by the counter-rotating lower and upper disks and separating two regions with opposite senses of azimuthal velocities. Two second-order recirculation zones due to Ekman pumping in the neighborhood of each disk (figure 1c) converge at mid-height and form an inward radial jet.

The geometry and basic state are axisymmetric and thus invariant under rotations  $S_{\theta_0}$  by angle  $\theta_0$  about the  $z$ -axis. The case  $s \equiv \Omega_{\text{up}}/\Omega_{\text{low}} = -1$  admits a supplementary symmetry of rotation of  $\pi$  about any horizontal axis, for example the  $x$ -axis, which we denote by  $R_\pi$ . This rotation is equivalent to combined reflections in  $\theta = 0$  and in  $z = 0$ .  $R_\pi$  does not commute with  $S_{\theta_0}$  and hence, the group generated by these operators is isomorphic to  $O(2)$ .

## 3. Numerical methods

Our primary goal is to carry out a linear stability analysis of the counter-rotating disk system for a range of aspect ratios. For this purpose, we have used a number of different

computational techniques: a steady state solver, linearized integration about a steady state, the ARPACK library (Lehoucq *et al.* (1998)) to compute leading eigenvalues and a nonlinear nonaxisymmetric code. The main features of these tools are summarized here. Further details can be found in Gadoin, Le Quéré & Daube (2001), Daube & Le Quéré (2002), Barbosa & Daube (2002) and Nore *et al.* (2003).

### 3.1. Spatial discretization

The flow fields are represented in cylindrical coordinates  $(r, \theta, z)$ . Fourier expansions are used in the  $\theta$ -direction while a staggered non-uniform grid with  $N_r + 1$  and  $N_z + 1$  gridpoints is used in the  $(r, z)$  plane. The grid is refined at the top, bottom and lateral boundaries and at the midplane as shown in figure 1d by placing gridpoints at:

$$r_i = \frac{\tanh\left(\frac{\beta i}{N_r}\right)}{\tanh(\beta)} \quad i = 0, \dots, N_r \quad (3.1a)$$

$$z_j = \frac{\Gamma}{4} \left( \frac{\tanh\left(\beta \left(\frac{2j - N_z/2}{N_z/2}\right)\right)}{\tanh(\beta)} + 1 \right) \quad j = 0, \dots, N_z/2 \quad (3.1b)$$

where  $\beta = 1.5$ . Formula (3.1b) is symmetrised under reflection in the midplane for the vertical gridpoints. The only unknown located on the axis  $r = 0$  is the axial component of the vorticity. The spatial discretization of the Navier-Stokes equations (2.1) uses mimetic finite difference operators (Hyman & Shashkov (1997)) and is an extension to non-uniform grids of the method described in Barbosa & Daube (2002).

Alongside the upper disk, at the points  $z = (z_{N_z/2} + z_{N_z/2-1})/2$ ,  $r < 1$  where  $v_\theta$  is computed, it is nearly  $-r\Omega$  and rapidly attains 0 at the shroud  $r = 1$ . A numerical gap can be defined as the distance  $\delta$  over which  $|v_\theta|$  attains half its maximum value. With our usual numerical treatment,  $\delta \simeq 0.0015$  for  $\Gamma = 0.5$ . To measure the influence of the junction singularity, we have also imposed a regularized boundary condition consisting of linearly interpolating  $v_\theta$  between  $\pm r\Omega$  at  $r_{N_r-3}$  and 0 at  $r_{N_r}$ . The resulting gap is  $\delta \simeq 0.0038$  and the linear thresholds of azimuthal modes  $m = 3, 4, 5$  differ by less than 0.03% from the non-regularized thresholds.

### 3.2. Axisymmetric steady states

Axisymmetric base flows are represented by the azimuthal velocity  $v$  and a streamfunction  $\psi$  defining the radial and vertical velocities via  $\nabla\psi \times \mathbf{e}_\theta/r$ . Temporal integration is first carried out to obtain a steady state at a low Reynolds number for which the basic axisymmetric state is stable. A Newton-Raphson method is used to calculate states at higher Reynolds numbers, which may be unstable to axisymmetric perturbations. In order to solve the large linear systems involved, we have used the Stokes preconditioned Newton method proposed in Tuckerman (1989) and Mamun & Tuckerman (1995), together with a matrix-free method, such as GMRES (Saad & Schultz (1986)). This preconditioned Newton method is very effective, provided that the full discrete coupled system is solved at each time step, rather than relying on approximations whose errors are proportional to some power of the time step  $\Delta t$ . Here, this is achieved by using an influence matrix technique in order to enforce the no-slip condition.

### 3.3. Linear stability analysis and time integration

A nonaxisymmetric code using primitive variables carries out both linear stability analysis and nonlinear time integration. The velocity components and pressure are expanded in truncated Fourier series over  $N_\theta$  modes in the azimuthal direction. Linear stability

	Resolution		Modes			
	$N_r$	$N_z$	0	1	2	3
Thresholds: present code	64	100	2699	3202	2526	3116
Gelfgat, Bar-Yoseph & Solan (2001)	30	30	2724	3217	2523	3119
Frequencies: present code	64	100	0.237	0.497	$\sim 0$	0.111
Gelfgat, Bar-Yoseph & Solan (2001)	30	30	0.2368	0.4949	0.0031	0.1104

TABLE 1. Thresholds and critical frequencies for azimuthal modes  $m = 0$  to 3 for a rotor-stator flow  $s = 0$  with  $\Gamma = 1.5$ .

analysis of a previously computed axisymmetric steady state  $\mathbf{V}$  is performed by time integration of the linearized Navier-Stokes equations:

$$\frac{\partial \mathbf{v}}{\partial t} + (\mathbf{V} \cdot \nabla) \mathbf{v} + (\mathbf{v} \cdot \nabla) \mathbf{V} = -\nabla p + \frac{1}{\text{Re}} \nabla^2 \mathbf{v} \quad (3.2a)$$

$$\nabla \cdot \mathbf{v} = 0 \quad (3.2b)$$

where homogeneous boundary conditions are imposed on  $\mathbf{v}$ . The temporal evolution of (2.1) or (3.2) is computed by a second-order implicit discretization of the linear terms and explicit Adams-Bashforth type extrapolation of the nonlinear terms (or their linearized version). The velocity–pressure coupling is handled by means of an incremental projection method (Goda (1979), Daube & Le Quéré (2002)).

For an axisymmetric basic state, the stability computation separates into a family of decoupled subproblems each associated with an azimuthal wavenumber  $m$ . Therefore linearized time-integration from an arbitrary initial condition corresponds to computing  $N_\theta$  integrations in parallel. The leading eigenvalues are extracted as half the slope of the evolution under (3.2) of the logarithm of the energy corresponding to each azimuthal wavenumber  $m$ . When needed, a limited number of leading eigenvalues of the linearized equations are computed by means of ARPACK, a software package based on an implicitly restarted Arnoldi method (Sorensen (1992), Lehoucq *et al.* (1998)).

The procedure is as follows. For a fixed aspect ratio  $\Gamma$ , a stable steady state at  $Re^0 = 100$  is computed using the axisymmetric temporal code. Successive axisymmetric steady states at  $Re = Re^0 + \Delta Re$  are calculated via Newton’s method. These steady states are substituted into the linearized Navier-Stokes equations (3.2), yielding the leading eigenvalue  $\lambda(m, Re, \Gamma) = \lambda_r(m, Re, \Gamma) + i\lambda_i(m, Re, \Gamma)$  for each azimuthal wavenumber  $m \leq N_\theta/2 - 1$ . The neutral Reynolds numbers  $Re_m(\Gamma)$  satisfy  $\lambda_r(m, Re_m(\Gamma), \Gamma) = 0$  and are determined by interpolation. The critical Reynolds number of the flow for each  $\Gamma$  is  $Re_C(\Gamma) \equiv \min_m Re_m(\Gamma)$ . The value of  $m$  corresponding to  $Re_C(\Gamma)$  is the critical mode  $m_C$ .

### 3.4. Code validation and resolution

Our code was tested by comparing our linearized computations with those by Gelfgat, Bar-Yoseph & Solan (2001) for the rotor-stator case  $s = 0$  and  $\Gamma = 1.5$ . Table 1 compares the thresholds and critical frequencies obtained with the resolution  $N_r = 64$ ,  $N_z = 100$  to those calculated by Gelfgat, Bar-Yoseph & Solan (2001) using spectral methods with  $30 \times 30$  basis functions which are linear superpositions of Chebychev polynomials. Our results agree to within 1% for the thresholds and within 0.5% for the frequencies.

---

$\Gamma$	Grid	Resolution		Modes					
		$N_r$	$N_z$	0	1	2	3	4	5
1.0	uniform	100	100	1332	420	299	312	387	533
1.0	non-uniform	64	100	1316	420	300	312	387	534
1.5	uniform	100	150	1607	332	309	426	653	892
1.5	non-uniform	64	100	1540	331	309	427	654	893
2.0	uniform	100	200	1852	349	400	625	909	1205
2.0	non-uniform	64	100	1842	349	401	625	910	1209
3.0	non-uniform	32	50	1929	495	647	1019	1427	1869
3.0	non-uniform	64	100	2156	504	656	1037	1441	1866
3.0	non-uniform	128	200	2172	507	659	1044	1449	1874

---

TABLE 2. Thresholds for azimuthal modes  $m = 0$  to 5 computed with uniform and non-uniform grids and with different resolutions for the counter-rotating disks  $s = -1$ .

---

We have performed convergence tests for  $s = -1$  and the tallest cylinder under investigation  $\Gamma = 3$  with three different resolutions. Results are reported in table 2. In this case, the resolution  $64 \times 100$  represents a compromise between accuracy and CPU time leading to errors in the thresholds of less than 0.7% for any wavenumber when compared with those of the finest mesh ( $128 \times 200$ ).

We have also compared the thresholds for three different aspect ratios obtained with the non-uniform grid (3.1) with those obtained using the uniform grid used in Nore *et al.* (2003). For the non-uniform grid, the same number of gridpoints is used for all aspect ratios, while for the uniform grid, the number of vertical gridpoints  $N_z$  is varied proportionately to the aspect ratio. For each aspect ratio, table 2 shows that the differences are less than 0.5%, except for the  $m = 0$  mode. The difficulty in resolving the  $m = 0$  instability is confirmed by a comparison with Gelfgat, Bar-Yoseph & Solan (1996), who found  $Re_0(\Gamma = 1.5) = 1644$  using an axisymmetric spectral code with  $40 \times 40$  basis functions, leading to a difference of 6.3% compared with our  $m = 0$  result for the resolution  $64 \times 100$ . In § 5, we will explain that the largest errors are located at values of  $\Gamma$  at which  $Re_0(\Gamma)$  undergoes very rapid change and that the seemingly large size of the error is in fact due to this effect. We will also compare the  $m = 0$  thresholds obtained with the temporal linear code and with ARPACK.

The results presented in this paper span the aspect ratio interval  $[0.5, 3]$ . For  $\Gamma = H/R < 1$ , we use more radial than vertical gridpoints and vice-versa for  $\Gamma \geq 1$ . More specifically, for  $1 \leq m \leq 5$ , computations are performed with  $N_r = 100$ ,  $N_\theta = 12$ ,  $N_z = 64$  for  $\Gamma < 1$  and with  $N_r = 64$ ,  $N_\theta = 12$ ,  $N_z = 100$  for  $\Gamma \geq 1$ . For  $m = 0$ , we have used an axisymmetric version of the non-uniform code with  $N_r = 200$ ,  $N_z = 128$  for  $\Gamma < 1$  and with  $N_r = 128$ ,  $N_z = 200$  for  $\Gamma \geq 1$ . The time step is  $\Delta t = 10^{-2}$  nondimensional time units for  $Re < 1000$  and  $\Delta t = 0.5 \times 10^{-2}$  for  $Re \geq 1000$ . A typical linear run of 50 disk rotations takes 500 seconds on a NEC-SX5 computer. About 30 linear runs are necessary to get the six thresholds for a fixed aspect ratio. Throughout the paper, we report thresholds as integer values of the Reynolds number.

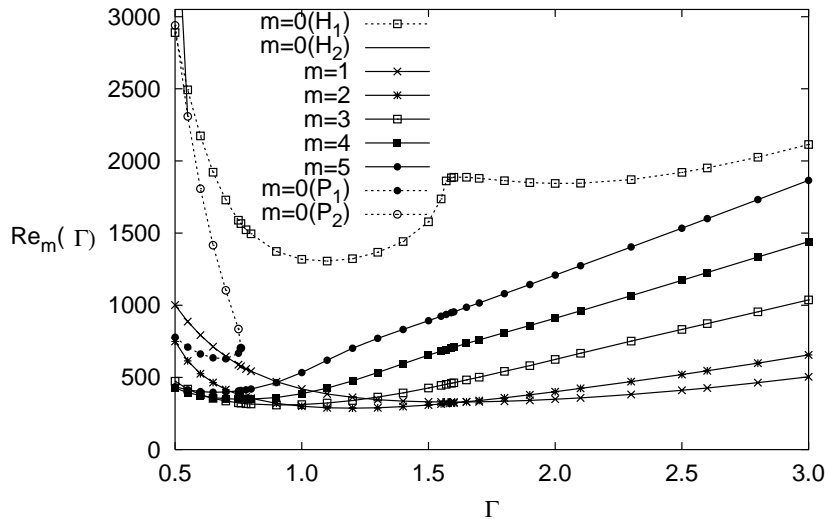


FIGURE 2. Thresholds  $Re_m(\Gamma)$  for azimuthal modes  $m = 0$  to 5 as functions of the aspect ratio  $\Gamma$ . The modes  $m = 1$  to 5 are stationary while the  $m = 0$  mode is stationary for  $m = 0$  ( $P_1$ ) and ( $P_2$ ) and oscillatory for  $m = 0$  ( $H_1$ ) and ( $H_2$ ).

---

wavenumber pair	$\Gamma$	$Re$
(4,3)	0.63	365
(3,2)	0.95	310
(2,1)	1.64	330

---

TABLE 3. Codimension-two points at which two azimuthal wavenumbers compete.

## 4. Three-dimensional modes

### 4.1. Thresholds and eigenvectors

We study the stability of the flow produced by counter-rotation of the bottom and top disks as a function of the aspect ratio in the range  $0.5 \leq \Gamma \leq 3$ . At each  $\Gamma$ , we compute the neutral Reynolds number given by  $Re_m(\Gamma)$  for integer values of the azimuthal wavenumber  $0 \leq m \leq 5$  (figure 2). All modes are stationary, i.e. the eigenvalues are zero at threshold, except for those on the branches denoted  $m = 0$  ( $H_1$ ) and  $m = 0$  ( $H_2$ ). The critical Reynolds number  $Re_C(\Gamma)$  is the lowest  $Re_m(\Gamma)$ , minimized over all  $m$ , and the corresponding azimuthal mode  $m_C$  is the most unstable mode. In the aspect ratio interval under consideration, the axisymmetric mode is never critical and its features differ substantially from those of the non-axisymmetric modes. We therefore begin by describing the  $m \neq 0$  mode results and defer description of the  $m = 0$  modes and thresholds to a separate section.

Figure 3a shows  $Re_C(\Gamma)$ , a lower envelope for the curves  $Re_m(\Gamma)$ , which yields the lowest threshold for each  $\Gamma$ . The critical Reynolds number  $Re_C(\Gamma)$  reaches its minimum value of 287 for  $\Gamma = 1.2$  and  $m = 2$ . The codimension-two points at which different azimuthal wavenumbers compete are shown in table 3.

The critical azimuthal mode  $m_C$  decreases with  $\Gamma$  or, equivalently, increases with  $1/\Gamma$ . This is seen in figure 3b, where the line  $m = 2.2R/H = 2.2/\Gamma$  has been drawn as a guide. One can observe that  $m_C \sim 1 + [2/\Gamma]$  where  $[ \cdot ]$  is the integer part of a real. This scaling

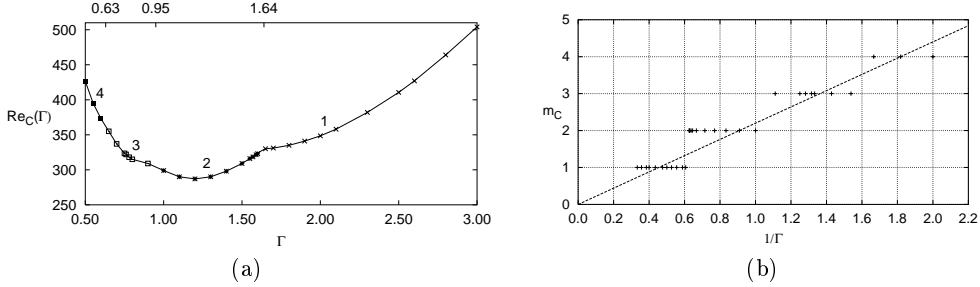


FIGURE 3. (a) Critical Reynolds number  $Re_C(\Gamma)$  as a function of  $\Gamma$  realised for different critical wavenumbers:  $m = 1$  ( $\times$ ),  $m = 2$  (\*),  $m = 3$  ( $\square$ ),  $m = 4$  ( $\blacksquare$ ). (b) Critical wavenumber  $m_C$  (+) as a function of the inverse of  $\Gamma$  with the indicative dashed line  $2.2/\Gamma$ .

for the first instability was already proposed in Nore *et al.* (2003) where it was postulated that the instability is located in the equatorial azimuthal shear layer occupying a constant proportion of the height, leading to an azimuthal wavelength which is half of the height.

To illustrate the three-dimensional patterns corresponding to the thresholds in figure 2 we choose four representative cases, with increasing critical wavenumbers  $m = 1, 2, 3, 4$ . For each case, we show contours of azimuthal velocity  $v$  and meridional vector field  $(u, w)$  of the unperturbed basic state and of the critical eigenvector. Isosurfaces of the perturbed velocity  $(u, v, w)$ , contours of  $w$  and unfolded contours of radial vorticity illustrate the azimuthal spatial distribution of the eigenvector.

As explained in § 2.2, the symmetry group of the counter-rotating disk system is isomorphic to  $O(2)$ . Each non-axisymmetric eigenmode is associated with a circle pitchfork bifurcation, producing a circle of steady states parameterized by angular phase  $\theta_0$ . Each eigenmode possesses a horizontal axis of symmetry; its orientation can be chosen so as to make the eigenmode symmetric under  $R_\pi$ . We illustrate this with figure 4(d), which shows vertical velocity contours of the  $m = 1$  eigenvector for  $\Gamma = 3$  at  $Re = 510$ , slightly above the bifurcation threshold  $Re_C = 504$ . At  $z = 0$ , the negative contours for  $0 < \theta < \pi$  correspond to the positive contours for  $\pi < \theta < 2\pi$ . The action of  $R_\pi$  relating contours at  $z = \Gamma/4$  and  $z = -\Gamma/4$  needs more work: choose a feature in the  $\Gamma/4$  plane, reflect it in  $\theta$ , take its opposite sign, and find it in the  $-\Gamma/4$  plane.

Another feature shared by all the eigenmodes is the equatorial location of the maximum disturbance. The isosurfaces (4c, 5c, 6c, 7c) lead to the conclusion that the radial localization evolves with the aspect ratio: for large  $\Gamma$ , the maximum disturbance is located near the vertical axis while, for small  $\Gamma$ , the largest gradients are concentrated at the periphery and are diffused by viscosity in the central region. As  $\Gamma$  decreases, the vorticity changes from helicoidal patterns to two families of spirals, one in each half from the equatorial plane. The spiral arms are directed in the sense of rotation of the nearest disk, preserving the  $R_\pi$  symmetry.

#### 4.2. Kelvin-Helmholtz mechanism

The radial vorticity of figures 4e, 5e, 6e and 7e resembles the disturbance that leads to the formation of co-rotating vortices, sometimes called cat's eyes, seen in the Kelvin-Helmholtz instability of a constant-vorticity shear layer. The number of vortices is the azimuthal critical wavenumber. Our observation of vortical structures motivates us to extend our interpretation of the instability of the basic axisymmetric flow as a manifestation of the Kelvin-Helmholtz instability (Nore *et al.* (2003)).

The Kelvin-Helmholtz instability is a two-dimensional instability of a basic velocity profile  $u(y)\mathbf{e}_x$  to perturbative modes  $(u'(y)\mathbf{e}_x + v'(y)\mathbf{e}_y)e^{i\alpha x}$ . Betchov & Szewczyk (1963)

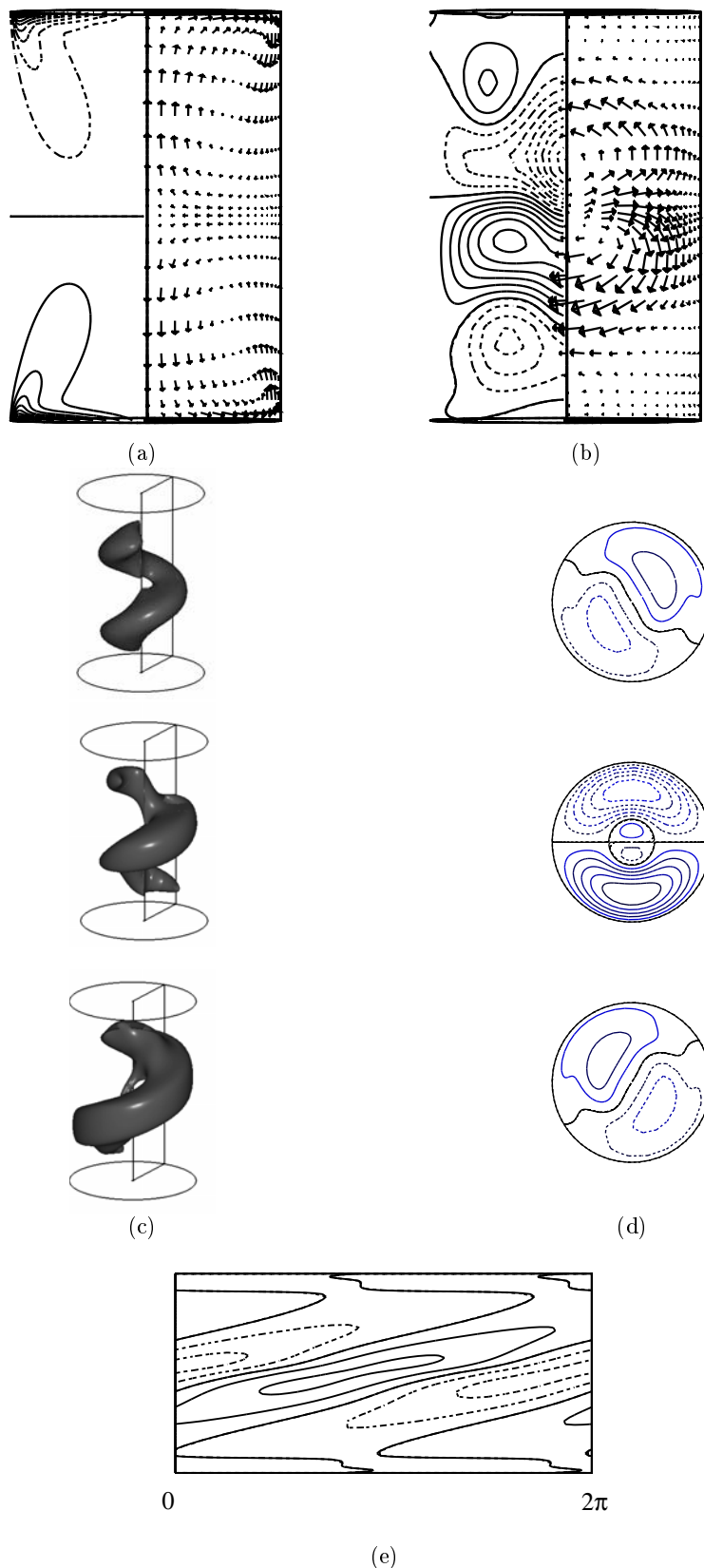


FIGURE 4. The  $m = 1$  eigenvector for  $\Gamma = 3$  and  $Re = 510$ . (a) Vector field with radial and vertical velocity components  $(u, w)$  at  $\theta = 0$  and contours of azimuthal velocity  $v$  at  $\theta = \pi$  for the basic state for comparison. (b) Vector field  $(u, w)$  at  $\theta_1 = 24^\circ$  and contours of  $v$  at  $\theta_2 = \pi + 24^\circ$  for the  $m = 1$  eigenvector. (c) Isosurface of  $u, v$  and  $w$  at one-quarter of the maximum positive value viewed slightly from above. (d) Vertical velocity contours at  $z = \Gamma/4$  (top),  $z = 0$  (middle), and  $z = -\Gamma/4$  (bottom) viewed from above. (e) Unfolded radial vorticity contours at  $r = 0.8$ . Positive (negative) values of a scalar function are indicated by solid (dashed) curves.

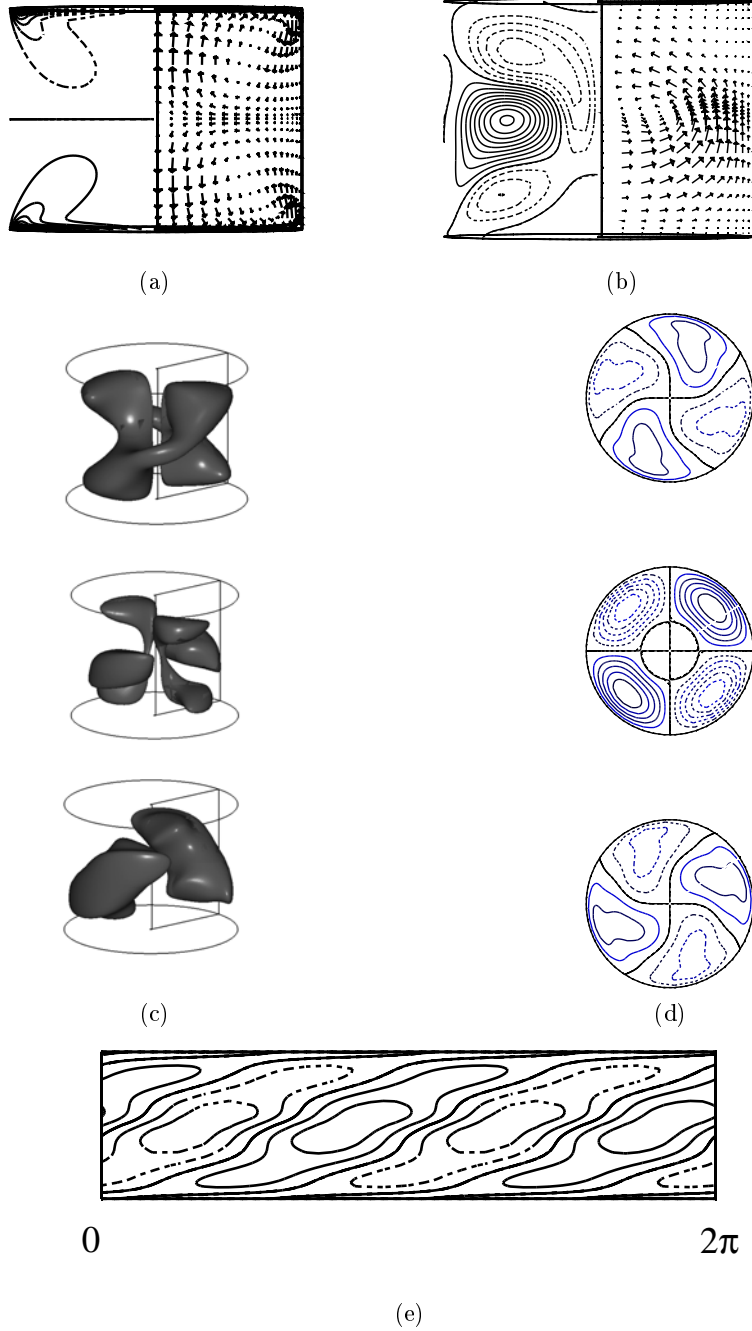


FIGURE 5. The  $m = 2$  eigenvector for  $\Gamma = 1.5$  and  $Re = 320$ . Same views as in figure 4, except (b)  $\theta_1 = 30^\circ$  and  $\theta_2 = \pi + 30^\circ$  and (e)  $r = 0.81$ .

studied the instability of the standard shear layer profile  $u(y) = U \tanh(y/\delta)$ . They computed the marginal stability curve in the  $(Re_{KH}, \alpha)$  plane, where  $Re_{KH} = U\delta/\nu$  and  $\alpha = 2\pi\delta/\lambda$  with  $\lambda$  the wavelength.

In our case, the basic profile is of the form  $v(r, z)\mathbf{e}_\theta$  and is perturbed by eigenmodes

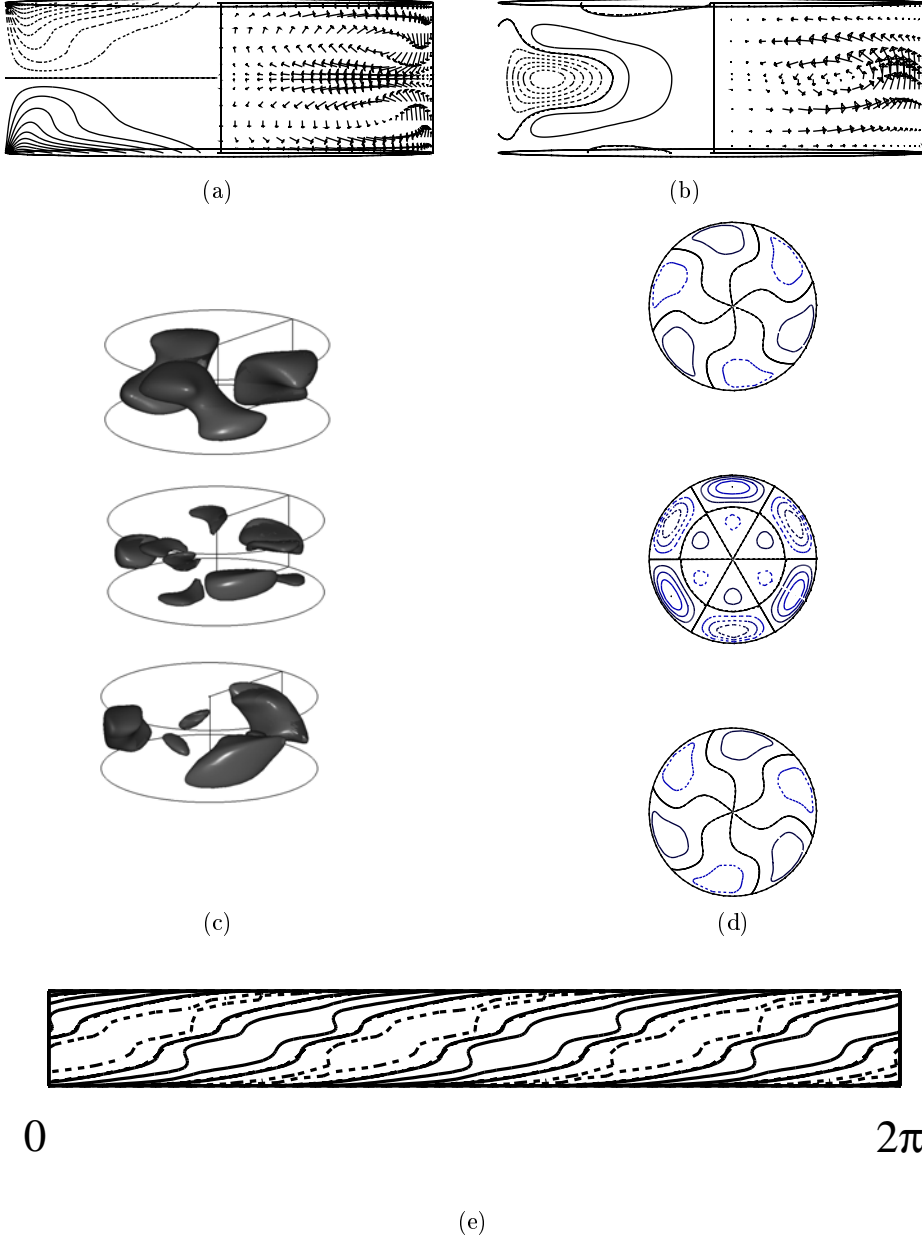


FIGURE 6. The  $m = 3$  eigenvector for  $\Gamma = 0.7$  and  $Re = 340$ . Same views as in figure 4, except (b)  $\theta_1 = -33^\circ$  and  $\theta_2 = \pi - 33^\circ$  and (e)  $r = 0.9$ .

such as  $(v'(r, z)\mathbf{e}_\theta + w'(r, z)\mathbf{e}_z)e^{im\theta}$ . The radial dependence is assumed to be weak and then treated as parametric. We fit the central portion of each basic state for the four cases of figures 4, 5, 6, 7 with a hyperbolic tangent function  $v(r, z)/r = \omega(r) \tanh(z/\delta(r))$ . For example, in figure 8a, for  $0.1 \lesssim r \lesssim 0.6$ , the profiles present vertical tangents at  $z \approx \pm 0.7$  and we apply the fit in this region. von Kármán (1921) and Batchelor (1951) derived a velocity profile for the axisymmetric flow between disks of infinite radii for which  $v(r, z)/r$  is independent of  $r$ . We have verified that this is approximately verified

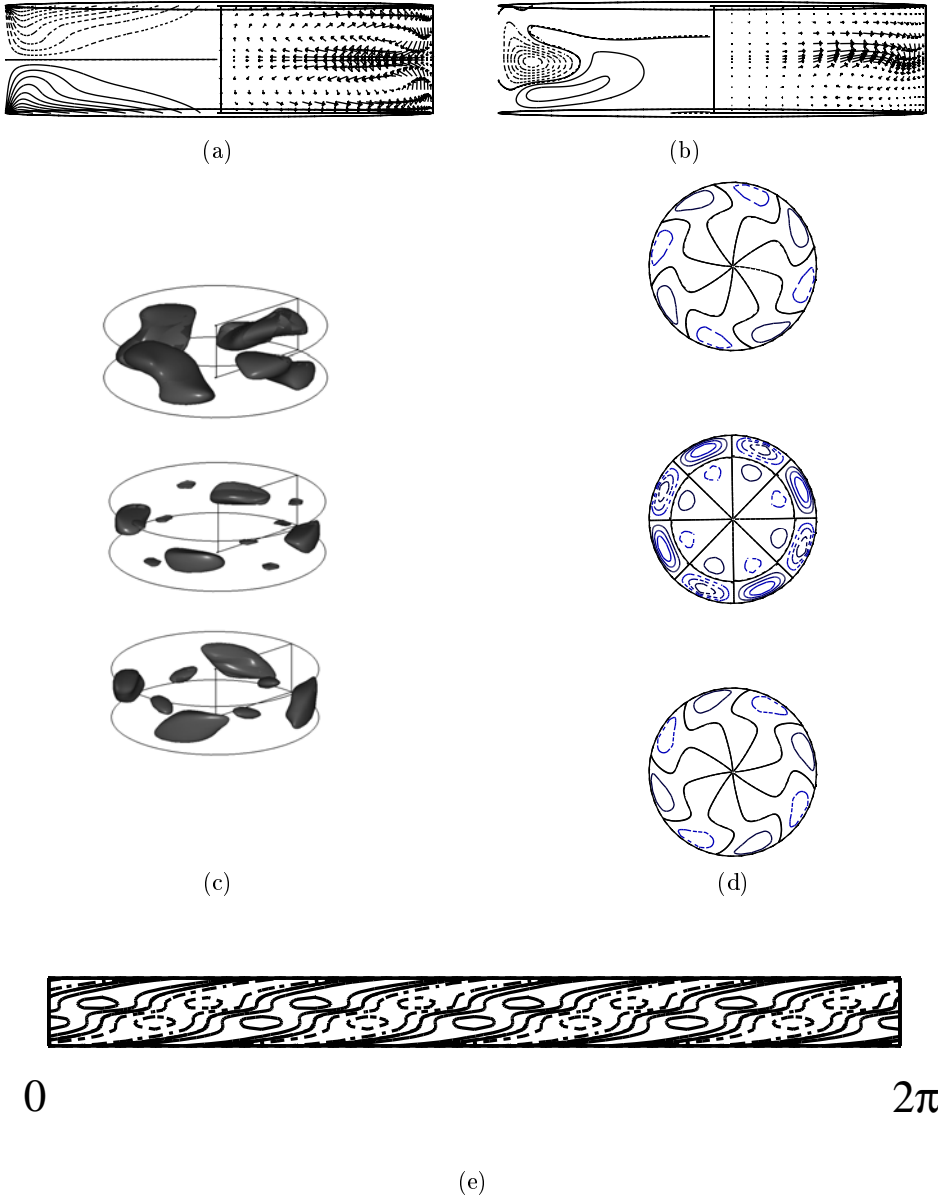


FIGURE 7. The  $m = 4$  eigenvector for  $\Gamma = 0.5$  and  $Re = 430$ . Same views as in figure 4, except (b)  $\theta_1 = -13^\circ$  and  $\theta_2 = \pi - 13^\circ$  and (e)  $r = 0.9$ .

for  $r$  between 0.1 and 0.6 at  $\Gamma = 3$ ; in particular  $\omega(r)$  and  $\delta(r)$  both remain close to 0.3. See also figure 27 of Nore *et al.* (2003).

We extend the analysis of Betchov & Szewczyk (1963) to  $Re_{KH}$  and  $\alpha$  depending on  $r$ , and a wavelength which is quantized by the finite circumference of the cylinder. We define

$$Re_{KH}(r) = r\omega(r)\delta(r)Re \quad \text{and} \quad \alpha(r) = \delta(r)m/r \quad (4.1)$$

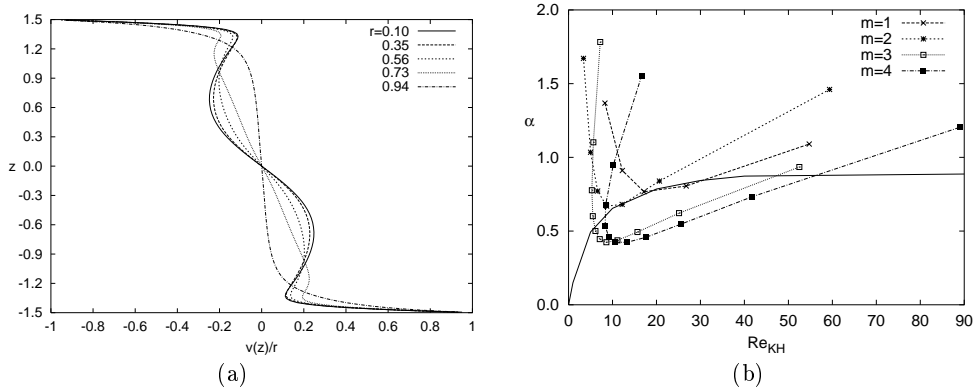


FIGURE 8. (a) Azimuthal profiles  $v(r, z)/r$  of the axisymmetric basic state for  $\Gamma = 3$  at  $Re = 510$  above the threshold  $Re_{m=1}(\Gamma = 3) = 504$  at different radii as indicated. The similarity zone, defined as the region in which the profiles  $v(r, z)/r$  depend only slightly on  $r$ , extends from  $r \sim 0.1$  to  $r \sim 0.6$ . (b) Wavenumber  $\alpha$  (in units of the inverse shear layer thickness) as a function of  $Re_{KH}$  computed for  $(m, \Gamma, Re) = (1, 3, 510)$ ,  $(m, \Gamma, Re) = (2, 1.5, 320)$ ,  $(m, \Gamma, Re) = (3, 0.7, 340)$ , and  $(m, \Gamma, Re) = (4, 0.5, 430)$ , just above their respective instability thresholds. For  $m = 1, 2, 3, 4$ , the  $r$  values shown are in the ranges  $[0.23, 0.65]$ ,  $[0.23, 0.80]$ ,  $[0.38, 0.89]$ , and  $[0.52, 0.94]$ , respectively, with  $r$  increasing from the left to the right endpoint of each curve. The marginal stability calculation of Betchov & Szewczyk (1963) is shown as the solid curve.

with  $\nu = 1/Re$  in our units and  $2\pi r/m$  the circumferential wavelength corresponding to azimuthal wavenumber  $m$  at a radius  $r$ . We calculate  $\omega(r)$  and  $\delta(r)$  for the basic axisymmetric velocity fields at a Reynolds number slightly above threshold for  $\Gamma = 3, 1.5, 0.7$  and  $0.5$  where the critical wavenumbers are 1, 2, 3 and 4, respectively. We then compute  $Re_{KH}(r)$  and  $\alpha(r)$  via (4.1). In figure 8b, we plot these points together with the marginal stability curve of Betchov & Szewczyk (1963); the Kelvin-Helmholtz unstable region is below this curve. It can be seen that, for each aspect ratio, the curve  $(Re_{KH}(r), \alpha(r))$  lies near or inside the Kelvin-Helmholtz unstable region for a radial interval depending on  $\Gamma$ . This analysis provides evidence that the mechanism responsible for the non-axisymmetric instabilities we have calculated is the Kelvin-Helmholtz instability.

#### 4.3. No 1:2 mode interaction at $\Gamma = 1.5$

The neutral curves of figure 2 determine the codimension-two point where the modes  $m = 1$  and  $m = 2$  bifurcate simultaneously at  $(\Gamma^*, Re^*) = (1.64, 330)$ . Near this point, the dynamics are described by the normal form (Armbruster, Guckenheimer & Holmes (1988)):

$$\dot{z}_1 = \overline{z}_1 z_2 + z_1 (\mu_1 + e_{11}|z_1|^2 + e_{12}|z_2|^2), \quad (4.2a)$$

$$\dot{z}_2 = \pm z_1^2 + z_2 (\mu_2 + e_{21}|z_1|^2 + e_{22}|z_2|^2), \quad (4.2b)$$

where  $z_1$  and  $z_2$  are complex amplitudes of the  $m = 1$  and  $m = 2$  modes. In a previous paper (Nore *et al.* (2003)), we have studied the dynamics at  $\Gamma = 2$ , where the mode  $m = 1$  bifurcates from the basic state before the mode  $m = 2$ . The two modes interact nonlinearly to create various complex flows as the Reynolds number is increased, such as stationary states with  $m = 1$  and  $m = 2$ , traveling waves, and near-heteroclinic cycles.

We now wish to investigate the nonlinear states which result when the order of the bifurcations is reversed. We thus choose for more detailed study the value  $\Gamma = 1.5 < \Gamma^*$  at which the mode  $m = 2$  bifurcates linearly at  $Re_C = 309$  before the mode  $m = 1$  at  $Re_{m=1} = 331$ . We have used the fully nonlinear version of the code described in sec-

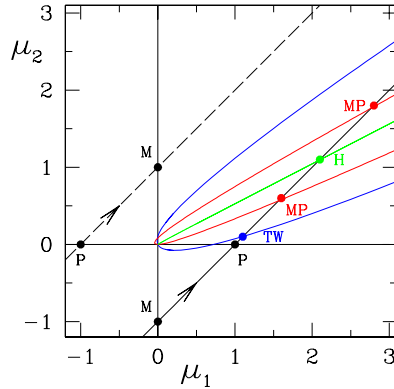


FIGURE 9. Phase diagram near the 1:2 codimension-two point. The two trajectories schematically represent increasing  $Re$  at two fixed values of  $\Gamma$  on either side of the codimension-two point at  $\Gamma^* = 1.64$ ,  $Re^* = 330$ . Lines  $M(m = 1)$ ,  $P(m = 2)$  indicate the locus of steady bifurcations from the axisymmetric state. Other curves indicate bifurcations to traveling waves ( $TW$ ), modulated traveling waves ( $H$ ), and between different steady states ( $MP$ ). Heteroclinic orbits exist between the two  $MP$  bifurcations. Time-dependent behavior occurs in a large region of parameter space when  $M$  is traversed before  $P$  ( $\Gamma > \Gamma^*$ , solid trajectory), but only extremely near the codimension-two point when the order is reversed ( $\Gamma < \Gamma^*$ , dashed trajectory).

tion §3.3 to compute nonlinear steady states with increasing  $Re$ . We obtain only the branch of  $m = 2$  steady states emanating from the supercritical pitchfork at  $Re_C$ . Attempts to produce behavior other than this by initializing the code with odd wavenumber components have not succeeded. It is only for  $Re > 900$ , far from the codimension-two point at  $Re^* = 330$ , that the  $m = 2$  branch undergoes an instability to an  $m = 1$  eigenvector and begins to show a change in spatial and temporal behavior. In contrast, Mercader, Prat & Knobloch (2002) observe near-heteroclinic cycles in their study of two-dimensional Rayleigh-Bénard convection with different boundary conditions at the top and bottom, for parameter values on either side of the 1:2 codimension-two point.

These results are consistent with figure 9 where complex behavior occurs almost exclusively in the  $\mu_1 > 0$ ,  $\mu_2 > 0$  quadrant and would be found only extremely near the codimension-two point when the  $m = 2$  precedes the  $m = 1$  instability. The coefficients  $e_{11} = -9$ ,  $e_{12} = -6$ ,  $e_{21} = -5$ , and  $e_{22} = -5$  of normal form (4.2) used in calculating figure 9 were chosen by Porter (private communication) because they lead to a sequence of bifurcations in qualitative agreement with the numerical results in Nore *et al.* (2003). These coefficients are apparently quite different from those pertaining to the Rayleigh-Bénard convection study of Mercader, Prat & Knobloch (2002).

## 5. Axisymmetric linear modes

Although the critical mode is never axisymmetric in the aspect ratio interval under consideration, our goal is to provide a complete survey of linear thresholds, which can be connected continuously to other ranges of  $\Gamma$  and  $s$ , where axisymmetric modes may become critical. For example, experimental results by Schouveiler, Le Gal & Chauve (1998), Gauthier, Gondret & Rabaud (1999), Schouveiler, Le Gal & Chauve (2001) show that, for small  $\Gamma$ , the bifurcation at threshold is to a system of concentric rolls.

Figure 10a represents the axisymmetric thresholds  $Re_0(\Gamma)$  as a function of  $\Gamma$  obtained

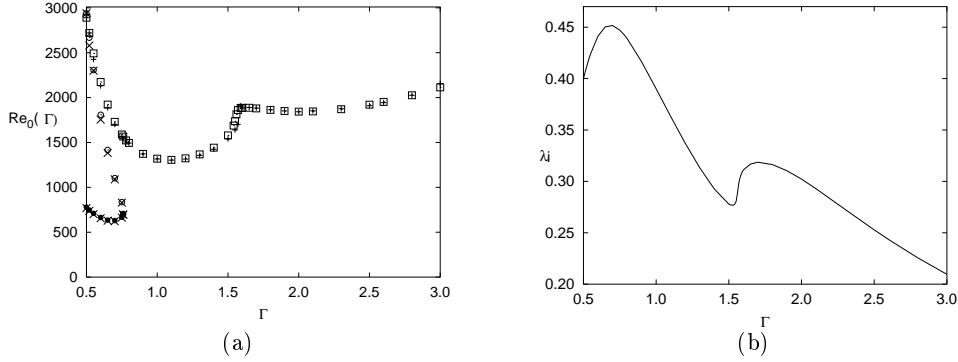


FIGURE 10. (a): Comparison of axisymmetric thresholds obtained with coarse and fine resolution. Pitchfork bifurcations  $P_1$ ,  $P_2$  are indicated by  $\bullet$ ,  $\circ$ ,  $\times$  and Hopf bifurcations  $H_1$  by  $\square$ ,  $+$ . Points  $\times$ ,  $+$  are computed with  $N_r = 100$ ,  $N_z = 64$  for  $\Gamma < 1$  and  $N_r = 64$ ,  $N_z = 100$  for  $\Gamma \geq 1$  while  $\bullet$ ,  $\circ$ ,  $\square$  are found using ARPACK with  $N_r = 200$ ,  $N_z = 128$  for  $\Gamma < 1$  and  $N_r = 128$ ,  $N_z = 200$  for  $\Gamma \geq 1$ . (b): Frequency  $\lambda_i(m = 0, Re_0(\Gamma), \Gamma)$  of  $H_1$  at threshold.

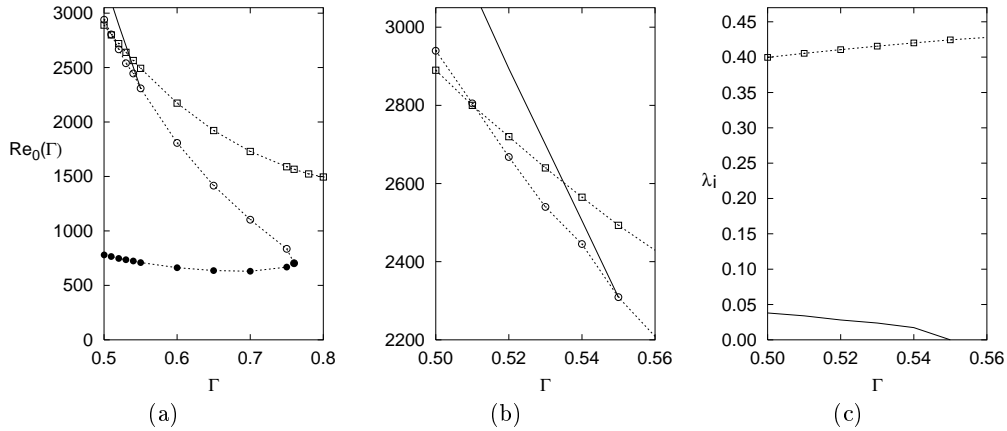


FIGURE 11. (a) Axisymmetric thresholds: two stationary bifurcations  $P_1$  ( $\bullet$ ) and  $P_2$  ( $\circ$ ) and two Hopf bifurcations  $H_1$  ( $\square$ ) and  $H_2$  ( $-$ ). (b) Enlargement for the thresholds for  $0.50 \leq \Gamma \leq 0.56$ . (c) Frequencies for  $H_1$  ( $\square$ ) and  $H_2$  ( $-$ ).

with a coarse and a fine resolution. This figure and the enlargements of figure 11 show up to four thresholds for each value of  $\Gamma$ . A Hopf bifurcation, denoted by  $H_1$ , exists throughout the range  $0.5 \leq \Gamma \leq 3.0$  that we have studied. Two pitchfork bifurcations, denoted by  $P_1$  and  $P_2$ , exist for  $0.50 \leq \Gamma < 0.78$ , merging and disappearing at  $\Gamma = 0.78$ ,  $Re = 700$ . Finally, another Hopf bifurcation,  $H_2$ , exists for  $0.50 \leq \Gamma \leq 0.55$ , and is annihilated when it meets  $P_2$  at  $\Gamma = 0.55$ ,  $Re = 2309$ . The termination of the  $H_2$  curve is a Takens-Bogdanov codimension-two bifurcation point, at which the frequency of  $H_2$  goes to zero, as shown in figure 11c.

This complicated evolution can be understood by plotting the growth rates  $\lambda_r(m = 0, Re, \Gamma)$  as a function of  $Re$  for different aspect ratios  $\Gamma$ , as shown in figure 12. Up to four leading  $m = 0$  eigenvalues computed using ARPACK (Lehoucq *et al.* (1998)) are represented on figure 12. For lower values of  $Re$ , the two leading eigenvalues are real; their intersections with the real axis when  $\Gamma < 0.78$  are responsible for the steady bifurcations  $P_1$  and  $P_2$ . These eigenvalues collide to form a complex conjugate pair whose real part is plotted on figure 12 and intersects the real axis when  $\Gamma < 0.55$ , leading to the Hopf

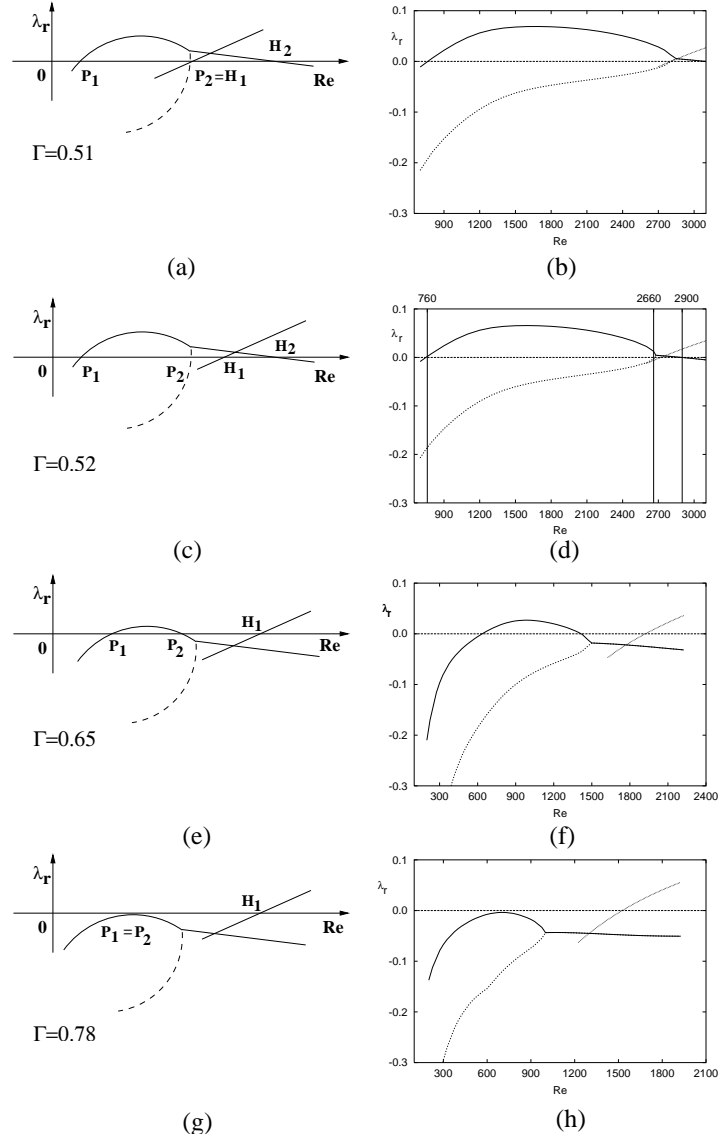


FIGURE 12. Growth rate  $\lambda_r(0, Re, \Gamma)$  of the four  $m = 0$  leading eigenvalues as a function of  $Re$  for different  $\Gamma$ . Left column, schematic diagrams, right column, computed values: (a,b)  $\Gamma = 0.51$ , (c,d)  $\Gamma = 0.52$ , (e,f)  $\Gamma = 0.65$  and (g,h)  $\Gamma = 0.78$ . Note that there are two stationary thresholds denoted as  $P_1$  and  $P_2$  for  $\Gamma < 0.78$ . These eigenvalues collide to form a complex conjugate pair whose real part is plotted and intersects the real axis when  $\Gamma < 0.55$ , leading to the Hopf bifurcation  $H_2$ . Another unrelated complex conjugate pair leads to another Hopf bifurcation  $H_1$  for  $0.5 \leq \Gamma \leq 3$ . Its imaginary part differs from those of the other eigenvalue branches, so the apparent intersections are not genuine, but rather an artifact of the projection onto the  $\lambda_r$  axis.

bifurcation  $H_2$ . Another unrelated complex conjugate pair is also shown on figure 12. Its real part overtakes that of the other eigenvalues for higher  $Re$  and intersects the real axis for all  $\Gamma$  values studied, leading to the Hopf bifurcation  $H_1$ . The imaginary part of the  $H_1$  pair is different from those of the other eigenvalues (except at  $\Gamma = 1.59$ ; see below), and hence the crossings seen on figure 12 do not correspond to actual intersections of this pair with other eigenvalues.

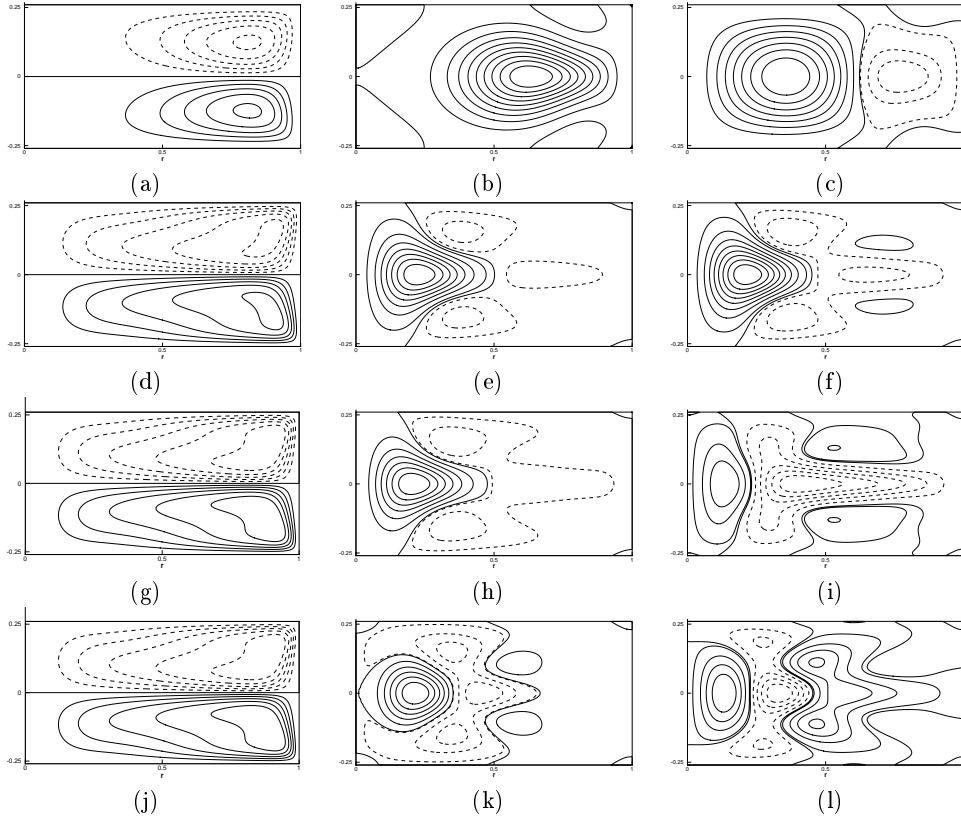


FIGURE 13. Streamfunction contours of axisymmetric states for  $\Gamma = 0.52$ . On the first row,  $Re = 760$ , near bifurcation  $P_1$ : (a) basic state; (b) the leading eigenvector responsible for the  $P_1$  bifurcation; (c) the second leading eigenvector. On the second row,  $Re = 2660$ , near bifurcation  $P_2$ : (d) basic state; (e) the leading eigenvector; (f) the second leading eigenvector responsible for the  $P_2$  bifurcation. On the third and fourth rows,  $Re = 2900$ : (g) basic state; (h,i) real and imaginary parts of the leading eigenpair responsible for the Hopf bifurcation  $H_2$ ; (j) basic state; (k,l) real and imaginary parts of the leading eigenpair responsible for the Hopf bifurcation  $H_1$ . See figure 12 (c,d) for this aspect ratio. Positive (negative) values are indicated by solid (dashed) curves.

On figure 13 streamfunction contours of the basic state and of the leading eigenvectors are plotted for the aspect ratio  $\Gamma = 0.52$  for Reynolds numbers near thresholds, at the parameter values indicated by vertical lines on figure 12d. The first two rows show real eigenvectors, the third and fourth rows complex eigenvectors. The basic state  $\Psi(r, z)$  is symmetric under  $R_\pi$ , while all eigenvectors  $\psi(r, z)$  are antisymmetric. At  $Re = 760$ , near the  $P_1$  bifurcation, the leading eigenvector (13b) contains one large cell while the second leading eigenvector (13c) also contains a second counter-rotating cell. On the second row, near the  $P_2$  bifurcation, the two leading eigenvectors (13e,f) resemble one another, containing two counter-rotating regions separated by a curved contour. This resemblance between these two eigenvectors is to be expected, since the Reynolds number  $Re = 2660$  is near that at which the real eigenvalues merge to form a complex pair (see figure 12d). The third and fourth rows of figure 13 show the basic state and real and imaginary components of the eigenvector responsible for the Hopf bifurcations  $H_2$  and  $H_1$ . The  $H_2$  eigenvector component (13h) resembles the real eigenvectors (13e,f) and its magnitude is

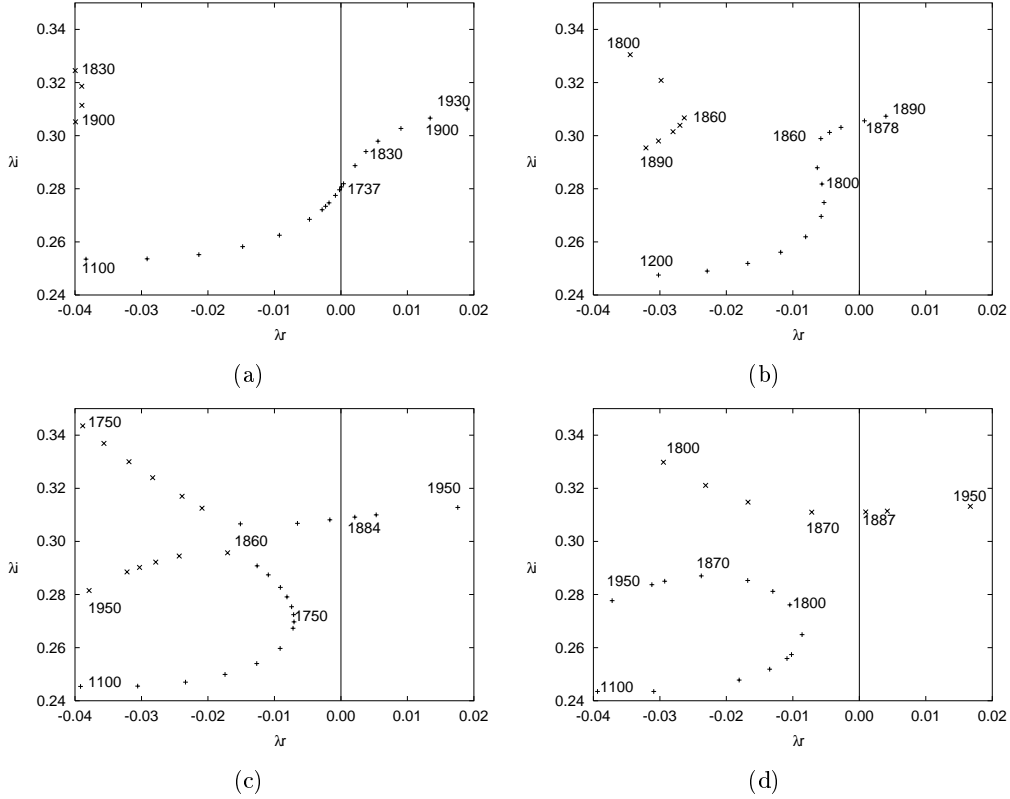


FIGURE 14. Real and imaginary parts of the two leading eigenvalues playing a role in the  $H_1$  Hopf bifurcation: (a)  $\Gamma = 1.55$ , (b)  $\Gamma = 1.58$ , (c)  $\Gamma = 1.59$ , (d)  $\Gamma = 1.6$ . The vertical line  $\lambda_r = 0$  defines the bifurcation threshold with  $\lambda_r = 0$ :  $Re_0(1.55) = 1737$ ,  $Re_0(1.58) = 1878$ ,  $Re_0(1.59) = 1884$  and  $Re_0(1.6) = 1887$ .

much larger than that of component (13i). The  $H_1$  eigenvector components (13k,l) look quite different.

We now examine the axisymmetric threshold at higher values of  $\Gamma$ . Figure 10a shows that  $Re_0(\Gamma)$  presents a rapid increase with  $\Gamma$  for  $\Gamma \lesssim 1.6$ , while it remains almost constant for  $\Gamma \gtrsim 1.6$ , with a corresponding variation in the frequency  $\lambda_i(m = 0, Re_0, \Gamma)$  at threshold. We have determined that this behavior is due to the crossing of the two leading eigenvalues, both complex. The intersection of complex eigenvalues, unlike that of real eigenvalues, is a codimension-two phenomenon: both  $\Gamma$  and  $Re$  must be adjusted in order to make the real and the imaginary parts of the two eigenvalues equal.

Figure 14 shows the evolution of the two leading eigenvalues in the  $(\lambda_r, \lambda_i)$  plane as  $Re$  is varied, for four different values of  $\Gamma$ . For  $\Gamma = 1.55$ , one eigenvalue branch extends across the diagram: the real part  $\lambda_r$  increases monotonically with  $Re$ , becoming positive at the  $H_1$  bifurcation at  $Re_0(1.55) = 1737$ . A second branch, with a higher  $\lambda_i$ , forms a loop at the left of the diagram, with a local maximum near  $\lambda_r \approx -0.04$ . By  $\Gamma = 1.58$ , the bifurcating eigenvalue branch has become folded into an S shape; an increasing portion of the branch is drawn into the  $\lambda_r < 0$  half-plane, postponing the  $H_1$  bifurcation to higher values of  $Re$  and of  $\lambda_i$ . At  $\Gamma = 1.59$ , the second eigenvalue branch joins with the first. Inspection of the eigenvectors corresponding to the two leading eigenvalues for  $\Gamma = 1.59$  and  $Re = 1880$  leads to the conclusion that the two eigenvectors are identical

---

Bifurcations	$\Gamma$	$Re$	Description
$H_1/P_2$	0.51	2802	
$H_1/H_2$	0.535	2602	
$H_2/P_2$	0.55	2309	Takens-Bogdanov point
$P_1/P_2$	0.78	700	isola formation point
$H_1$	1.59	1860	intersection of two complex eigenvalues

---

TABLE 4. Axisymmetric codimension-two points.

at the crossing. This reconnection leads to the discontinuities in the derivatives of the threshold and frequency curves in figures 10. The curves seen in figure 14 illustrate the way in which the roots of a cubic polynomial cross one another as the coefficients of the polynomial are varied. (This evolution is familiar in the dynamical-systems context from the unfolding of a transcritical bifurcation.) All the codimension-two points involving the axisymmetric modes are listed in table 4.

The nearly vertical tangent of the threshold curve near  $\Gamma = 1.6$  in figure 10a explains the discrepancy between our thresholds and those of Gelfgat, Bar-Yoseph & Solan (1996) (see § 3.4). Figure 10a compares the axisymmetric thresholds  $Re_0(\Gamma)$  obtained with a coarse and a fine resolution. The largest difference between the two resolutions, 8.6%, occurs near  $\Gamma = 1.6$ , where the variation of the Hopf thresholds is greatest. This is because  $\Delta Re/\Delta\Gamma \rightarrow \infty$  for  $\Gamma \sim 1.6$ ; a consequence of this is that for a fixed aspect ratio, the thresholds between the two resolutions can differ by an  $O(1)$  value. Conversely, the variation of  $\Gamma$  with Reynolds number is such that  $\Delta\Gamma/\Delta Re \rightarrow 0$ . Indeed, when figure 10a is interpreted as describing a function  $\Gamma_C(Re)$ , i.e. when the differences are taken horizontally rather than vertically, the results from the two resolutions agree to within 1.8% in  $\Gamma$ . Similar conclusions apply near  $\Gamma = 0.5$ , where the threshold also varies rapidly. Consequently, figure 10a shows that the spatial resolution we have used is adequate.

## 6. Conclusion

We have determined the linear three-dimensional instabilities of the flow between exactly counter-rotating disks over the aspect ratio range  $\Gamma = H/R \in [0.5, 3]$  with azimuthal wavenumber  $m \leq 5$ . The dynamics are dominated by the instability of the equatorial shear layer following the physical mechanism of the Kelvin-Helmholtz instability. The roll-up of the shear layer gives rise to stationary radial vortices along the static periphery. We have determined the critical azimuthal wavenumber corresponding to each value of  $\Gamma$  and established the approximate law  $m_C \sim 2.2/\Gamma$ : the greater the non-dimensional radius, the greater the number of vortices formed. This is consistent with the simple rule that each vortex occupies half of the cylinder height.

The stationarity of the vortices is a consequence of the symmetry of the configuration and of the basic flow: the rotation speeds of the upper and lower disks are equal and opposite. This makes the system invariant under rotation by  $\pi$  about any horizontal axis, as well as any rotation about the vertical axis, leading to the symmetry group  $O(2)$ . An experiment using a water-glycerol mixture is planned to check our predictions. Any experimental imperfection will break the  $R_\pi$  invariance, thus leaving only the  $SO(2)$  group of rotations about the vertical axis, which leads generically to rotating patterns (Knobloch (1993)). Our challenge will be to obtain experimentally stationary vortices and to study the shape of these axisymmetry-breaking structures.

We have located the 1:2 codimension-two point at which the  $m = 1$  and  $m = 2$  thresholds coincide as  $\Gamma^* = 1.64$ ,  $Re^* = 330$ . In a previous paper (Nore *et al.* (2003)), we studied the sequence of nonlinear states which occur as  $Re$  is varied near this codimension-two point for  $\Gamma = 2$ , where the  $m = 1$  threshold precedes that of  $m = 2$ . These states included traveling waves and robust heteroclinic cycles. For  $\Gamma = 1.5$ , where the  $m = 2$  threshold precedes that of  $m = 1$ , no such states occur.

For  $0.5 \leq \Gamma \leq 3$ , the first instability is never axisymmetric; we have nevertheless computed  $m = 0$  thresholds for completeness and in the hope of connecting these to primary axisymmetric instabilities at other parameter values. The sequence of axisymmetric instabilities is quite complicated, involving a pair of pitchfork bifurcations and two Hopf bifurcations, which succeed one another via various codimension-two points. Over most of the range studied, there exists only one axisymmetric instability, a Hopf bifurcation, the steep variation of whose threshold with  $\Gamma$  poses theoretical and numerical challenges.

We gratefully acknowledge Yann Fraigneau for his technical assistance, Alexander Gelfgat for providing his results reported in table 1 and Dwight Barkley for helpful discussions. The computations were carried out on the NEC-SX5 computer of the Institut du Développement et des Ressources en Informatique Scientifique (IDRIS) of the Centre National pour la Recherche Scientifique (CNRS) (project # 0254).

#### REFERENCES

- ARMBRUSTER D., GUCKENHEIMER J. & HOLMES P. 1988 Heteroclinic cycles and modulated traveling waves in systems with  $O(2)$  symmetry. *Physica D* **29**, 257–282.
- BARBOSA E. & DAUBE O. 2002 A finite differences method in cylindrical coordinates for 3D incompressible flows. *submitted to J. Comp. Phys.*
- BATCHELOR G.K. 1951 Note on a class of solutions of the Navier-Stokes equations representing steady rotationally-symmetric flow. *Q. J. Mech. Appl. Math.* **4**, 29–41.
- BETCHOV R. & SZEWCZYK A. 1963 Stability of a shear layer between parallel streams. *Phys. Fluids* **6**, 1391–1396.
- BLACKBURN H. M. & LOPEZ J. M. 2000 Symmetry breaking of the flow in a cylinder driven by a rotating end wall. *Phys. Fluids* **12**, 2698–2701.
- BLACKBURN H. M. & LOPEZ J. M. 2002 Modulated rotating waves in an enclosed swirling flow. *J. Fluid Mech.* **465**, 33–58.
- COUSIN-RITTEMAR D., DAUBE O. & LE QUÉRÉ P. 1998 Sur la nature de la première bifurcation des écoulements interdisques. *C. R. Acad. Sc. Paris* **326**, 359–366.
- CRAWFORD J.D. & KNOBLOCH E. 1991 Symmetry and symmetry-breaking bifurcations in fluid dynamics. *Annu. Rev. Fluid Mech.* **23**, 342–388.
- DAUBE O. & LE QUÉRÉ P. 2002 Numerical investigation of the first bifurcation for the flow in a rotor-stator cavity of radial aspect ratio 10. *Computers & Fluids* **31**, 481–494.
- ESCUDIER M. P. 1984 Observations of the flow produced in a cylindrical container by a rotating endwall. *Exps. Fluids* **2**, 189–196.
- FALLER A.J. 1991 Instability and transition of disturbed flow over a rotating disk *J. Fluid Mech.* **230**, 245–269.
- GADOIN E., LE QUÉRÉ P. & DAUBE O. 2001 A general methodology to investigate flow instabilities in complex geometries : application to natural convection in enclosures. *Int. J. Num. Meth. in Fluids* **37**, 175–208.
- GAUTHIER G., GONDRET P., MOISY F. & RABAUD M. 2002 Instabilities of the flow between co and counter-rotating disks *J. Fluid Mech.* **473**, 1–21.
- GAUTHIER G., GONDRET P. & RABAUD M. 1999 Axisymmetric propagating vortices in the flow between a stationary and a rotating disk enclosed by a cylinder. *J. Fluid Mech.* **386**, 105–126.
- GELFGAT Y.A., BAR-YOSEPH P.Z. & SOLAN A. 1996 Steady states and oscillatory instability of swirling flow in a cylinder with rotating top and bottom. *Phys. Fluids* **8**, 2614–2625.

- GELFGAT Y.A., BAR-YOSEPH P.Z. & SOLAN A. 2001 Three-dimensional instability of axisymmetric flow in a rotating lid-cylinder enclosure. *J. Fluid Mech.* **438**, 363–377.
- GODA K. 1979 A multistep technique with implicit difference schemes for calculating two- or three-dimensional cavity flows. *J. Comp. Phys.* **30**, 76–95.
- HENDERSON R.D. & BARKLEY D. 1996 Secondary instability in the wake of a circular cylinder. *Phys. Fluids* **8**, 1683–1685.
- HYMAN J.M. & SHASHKOV M. 1997 Natural discretizations for the divergence, gradient and curl on logically rectangular grids. *Comp. Math. Applic.* **33**, 81–104.
- VON KÁRMÁN T. 1921 Über laminare und turbulente Reibung. *Z. Angew. Math. Mech.* **1**, 233–252.
- KNOBLOCH E. 1993 Bifurcations in Rotating Systems. *Theory of Solar and Planetary Dynamos: Introductory Lectures*, Ed. M.R.E. Proctor and A. D. Gilbert, Cambridge Univ. Press.
- KUZNETSOV Y.A. 1998 *Elements of Applied Bifurcation Theory*, (Springer, New York).
- LEHOUCQ R.B., SORENSEN D.C. & YANG C. 1998 *ARPACK User's Guide, Philadelphia (SIAM, Philadelphia)*.
- LOPEZ J.M., MARQUES F. & SANCHEZ J. 2001 Oscillatory modes in an enclosed swirling flow. *J. Fluid Mech.* **439**, 109–129.
- LOPEZ J.M., HART J.E., MARQUES F., KITTELMAN S. & SHEN J. 2002 Instability and mode interactions in a differentially-driven rotating cylinder. *J. Fluid Mech.* **462**, 383–409.
- MAMUN C.K. & TUCKERMAN L. S. 1995 Asymmetry and Hopf bifurcation in spherical Couette flow. *Phys. Fluids* **7**, 80–91.
- MERCADER I., PRAT J. & KNOBLOCH E. 2002 Robust heteroclinic cycles in two-dimensional Rayleigh-Bénard convection without Boussinesq symmetry. *Int. J. Bif. Chaos* **12** 2501–2522.
- MOISY F., DOARÉ O., PASUTTO T., DAUBE O. & RABAUD M. 2003 Experimental and numerical study of the shear layer instability between two counter-rotating disks submitted to *J. Fluid Mech.*
- NORE C., TUCKERMAN L.S., DAUBE O. & XIN S. 2003 The 1 : 2 mode interaction in exactly counter-rotating von Kármán swirling flow. *J. Fluid Mech.* **477**, 51–88.
- PIKHTOV S.V. & SMIRNOV E.M. 1993 Boundary layer stability on a rotating disk with corotation of the surrounding fluid *Fluid. Dyn.* **27**, 657–663.
- PORTER, J., private communication.
- SAAD Y. & SCHULTZ M.H. 1986, GMRES: a generalized minimal residual algorithm for solving nonsymmetric linear systems. *S.I.A.M. J. Sci. Stat. Comput.*, **7**, 856–869.
- SCHOUVEILER L., LE GAL P. & CHAUVE M.-P. 1998 Stability of a traveling roll system in a rotating disk flow. *Phys. Fluids* **10**, 2695–2697.
- SCHOUVEILER L., LE GAL P. & CHAUVE M.-P. 2001 Instabilities of the flow between a rotating and a stationary disk. *J. Fluid Mech.* **443**, 329–350.
- SERRE E., CRESPO DEL ARCO E. & BONToux P. 2001 Annular and spiral patterns in flows between rotating and stationary disks. *J. Fluid Mech.* **434**, 65–100.
- SORENSEN D.C. 1992 Implicit Application of Polynomial Filters in a k-Step Arnoldi Method. *S.I.A.M.* **13**, 357–385.
- SOTIROPOULOS F. & VENTIKOS Y. 1998 Transition from bubble-type vortex breakdown to columnar vortex in a confined swirling flow. *Int. J. Heat and Fluid Flow* **19**, 446–458.
- SOTIROPOULOS F. & VENTIKOS Y. 2001 The three-dimensional structure of confined swirling flows with vortex breakdown. *J. Fluid Mech.* **426**, 155–175.
- SPOHN A., MORY M. & HOPFINGER E. J. 1998 Experiments on vortex breakdown in a confined flow generated by a rotating disk. *J. Fluid Mech.* **370**, 73–99.
- TUCKERMAN L.S. 1989 Steady-state solving via Stokes preconditioning: Recurrence relations for elliptic operators. *Lecture notes in Physics*, Dwoyer D.L., Hussaini M.Y. and Voigt R.G., Springer.
- ZANDBERGEN P. J. & DIJKSTRA D. 1987 Von Kármán swirling flows. *Annu. Rev. Fluid Mech.* **19**, 465–491.